



Contents lists available at ScienceDirect

## Remote Sensing of Environment

journal homepage: [www.elsevier.com/locate/rse](http://www.elsevier.com/locate/rse)

## Evaluating Landsat 8 evapotranspiration for water use mapping in the Colorado River Basin

Gabriel B. Senay<sup>a,\*</sup>, MacKenzie Friedrichs<sup>b,1</sup>, Ramesh K. Singh<sup>c,1,2</sup>, Naga Manohar Velpuri<sup>c,1,2</sup>

<sup>a</sup> U.S. Geological Survey (USGS), Earth Resources Observation and Science (EROS) Center, North Central Climate Science Center, Fort Collins, CO, USA

<sup>b</sup> SGT Inc., Contractor to the USGS EROS Center, Sioux Falls, SD, USA

<sup>c</sup> ASRC InuTeq LLC, Contractor to the USGS EROS Center, Sioux Falls, SD, USA

### ARTICLE INFO

#### Article history:

Received 25 April 2015

Received in revised form 10 December 2015

Accepted 30 December 2015

Available online xxxxx

#### Keywords:

Evapotranspiration

SSEBop model

Landsat

ET modeling

Colorado River Basin

### ABSTRACT

Evapotranspiration (ET) mapping at the Landsat spatial resolution (100 m) is essential to fully understand water use and water availability at the field scale. Water use estimates in the Colorado River Basin (CRB), which has diverse ecosystems and complex hydro-climatic regions, will be helpful to water planners and managers. Availability of Landsat 8 images, starting in 2013, provides the opportunity to map ET in the CRB to assess spatial distribution and patterns of water use. The Operational Simplified Surface Energy Balance (SSEBop) model was used with 528 Landsat 8 images to create seamless monthly and annual ET estimates at the inherent 100 m thermal band resolution. Annual ET values were summarized by land use/land cover classes. Croplands were the largest consumer of “blue” water while shrublands consumed the most “green” water. Validation using eddy covariance (EC) flux towers and water balance approaches showed good accuracy levels with  $R^2$  ranging from 0.74 to 0.95 and the Nash–Sutcliffe model efficiency coefficient ranging from 0.66 to 0.91. The root mean square error (and percent bias) ranged from 0.48 mm (13%) to 0.60 mm (22%) for daily (days of satellite overpass) ET and from 7.75 mm (2%) to 13.04 mm (35%) for monthly ET. The spatial and temporal distribution of ET indicates the utility of Landsat 8 for providing important information about ET dynamics across the landscape. Annual crop water use was estimated for five selected irrigation districts in the Lower CRB where annual ET per district ranged between 681 mm to 772 mm. Annual ET by crop type over the Maricopa Stanfield irrigation district ranged from a low of 384 mm for durum wheat to a high of 990 mm for alfalfa fields. A rainfall analysis over the five districts suggested that, on average, 69% of the annual ET was met by irrigation. Although the enhanced cloud-masking capability of Landsat 8 based on the cirrus band and utilization of the Fmask algorithm improved the removal of contaminated pixels, the ability to reliably estimate ET over clouded areas remains an important challenge. Overall, the performance of Landsat 8 based ET compared to available EC datasets and water balance estimates for a complex basin such as the CRB demonstrates the potential of using Landsat 8 for annual water use estimation at a national scale. Future efforts will focus on (a) use of consistent methodology across years, (b) integration of multiple sensors to maximize images used, and (c) employing cloud-computing platforms for large scale processing capabilities.

Published by Elsevier Inc. This is an open access article under the CC BY license (<http://creativecommons.org/licenses/by/4.0/>).

### 1. Introduction

Water management principles and techniques are required to optimize the beneficial uses of the available water resources to meet human and ecological needs. Critical elements of water management include knowledge of supply and demand along with the spatiotemporal dynamics of the sources (e.g., reservoirs, streams, wells) and uses

(e.g., irrigation, power generation, and domestic supply). Since 1950, the U.S. Geological Survey (USGS) has published national estimates of water use at 5-year intervals using varied data sources such as pumping, crop coefficients, and withdrawals, with all having different levels of accuracy (Holland, 1992; Solley, Merk, & Pierce, 1988). In 1977, the USGS National Water-Use Information Program (NWUIP) was established to produce more uniformly acquired water use data using guidelines and standards to meet regional and national needs from data aggregated at the county level (Mann, Moore, & Chase, 1982).

Although NWUIP improved the quality of water use information by standardizing the terminology, definition, and categories of water use (irrigation, power generation, domestic, etc.) that are adopted by the water use collecting agencies (federal, state, and local), NWUIP faced

\* Corresponding author at: USGS EROS Center, Colorado State University, Fort Collins, CO 80523-1499, USA.

E-mail address: [senay@usgs.gov](mailto:senay@usgs.gov) (G.B. Senay).

<sup>1</sup> Contractor to the USGS EROS Center.

<sup>2</sup> Work performed under USGS contract G10PC00044 in support of the WaterSMART initiative.

several challenges in obtaining accurate and timely information, partly attributable to the varying methods of water use estimation used for each category by different states and agencies (Maupin et al., 2014). For example, since 2000, NWUIP discontinued the estimation and reporting of return flow (the portion of water returning to the source after a point of application) and consumptive use (the fraction of water removed from subsequent availability due to evapotranspiration or incorporation into products) due to data constraints (Maupin et al., 2014).

According to the most recent nationwide 5-year water use compilation (based on withdrawal information), 2010 had the lowest annual consumptive use in the United States since 1970 (Maupin et al., 2014). With a total water withdrawal of 491 billion m<sup>3</sup>/year (bm<sup>3</sup>/year) or 355 billion gallons per day (bgal/d), 2010 water withdrawal was 13% lower than that during 2005, with 86% and 14% split between freshwater and saline-water sources, respectively. The two largest water users remained thermoelectric and irrigation in 2010. Withdrawal for thermoelectricity accounted for 45% of total water withdrawals (fresh and saline sources), with 38% of the total withdrawal from freshwater sources.

On the other hand, irrigation (all freshwater, a total of 159 bm<sup>3</sup>/year or 115 bgal/d) accounted for 38% of total withdrawal for all uses, or 61% of total water use excluding thermoelectric, and represented the lowest total irrigation water withdrawal since 1965 (Maupin et al., 2014).

To place the 2010 total withdrawal in perspective, the 491 bm<sup>3</sup>/year withdrawal is equivalent to 24.6 times the mean (1906–2012) annual flow (natural) of the Colorado River (19.94 bm<sup>3</sup>/year or 16.16 ac-ft, (USBR, 2015) at a point above the Imperial Dam (USGS stream gage number 09429490) located at the border of California and Arizona. Although the natural flow of the river reaches close to 20 bm<sup>3</sup>/year, the actual annual flow volume leaving the border to Mexico is small with the minimum set at 1.85 bm<sup>3</sup>/year (1.5 million ac-ft) (USBR, 2015). The balance is allocated and used to meet various water use demands, from irrigation in the basin to industrial use and domestic water supply in the major cities of the Southwest.

One of the challenges of estimating actual water use by irrigation using withdrawal data is that different crops use water at different rates in a given location, and the same crop uses water differently in a different climatic setting within the same basin. Furthermore, irrigation efficiencies related to the conveyance type (lined versus unlined canals) and application methods (surface versus sprinkler) bring large disparities in estimating crop consumptive use using total withdrawal amounts.

The USGS National Water Census research program is focused on developing new tools to quantify and map evapotranspiration (ET) for two major purposes: (1) estimating crop water use at a county level to support the NWUIP's requirements, and (2) estimating basin-scale water availability (relative proportion of the different water balance components in a watershed) at the hydrologic unit code (HUC) 12 level for the entire nation. Although daily estimates of ET are desired for both objectives, the initial goal is to produce seasonal ET estimates for the previous year by April of a given year. Thus, knowledge of irrigation water use of the previous year can be used for assessing water use needs for the upcoming crop growing season (May to September). The USGS National Water Census is implemented as part of the Department of Interior's WaterSMART (Sustain and Manage America's Resources for Tomorrow) initiative on water use and availability (DOI, 2011).

Remote sensing approaches for estimating evapotranspiration are gaining prominence for their large area coverage using a consistent dataset and the capability to map the spatial variability of ET at subfield scales. Evapotranspiration is an important process in the hydrologic cycle. Among the major water budget components, ET is in a gaseous state as opposed to precipitation and streamflow, making it the most difficult component to measure directly. ET comprises two sub-

processes: (1) evaporation from the soil and vegetation surfaces and (2) transpiration from the plants. Consequently, ET plays a major role in the exchange of mass and energy between the soil-water-vegetation system and the atmosphere. Knowledge of the rate and amount of ET for a given location is an essential component in the design, development, and monitoring of hydrologic, agricultural, and environmental systems.

Several methods for remotely sensed ET of irrigated fields located under uniform hydro-climatic regions have been shown to be reliable. These methods include the Surface Energy Balance Index (SEBI) (Menenti & Choudhury, 1993), Two Source Model (TSM) (Norman, Kustas, & Humes, 1995), Surface Energy Balance Algorithm for Land (SEBAL) (Bastiaanssen, Menenti, Feddes, & Holtlag, 1998), Simplified Surface Energy Balance Index (S-SEBI) (Roerink, Su, & Menenti, 2000), Surface Energy Balance System (SEBS) (Su, 2002), ET Mapping Algorithm (ETMA) (Loheide & Gorelick, 2005), Atmosphere-Land Exchange Inverse (ALEXI) (Anderson, Norman, Mecikalski, Otkin, & Kustas, 2007), Mapping Evapotranspiration at high Resolution with Internalized Calibration (METRIC) (Allen, Tasumi, & Trezza, 2007), Simplified Surface Energy Balance (SSEB) (Senay, Budde, Verdin, & Melesse, 2007) and wet METRIC (wMETRIC) (Singh & Irmak, 2011). Reviews of these and other methods for estimating ET using remotely sensed data are presented by other researchers (Allen, Pereira, Howell, & Jensen, 2011; Glenn, Neale, Hunsaker, & Nagler, 2011; Gowda et al., 2007; Kalma, McVicar, & McCabe, 2008). The choice of ET model and input data is likely to have a bearing on model performance at geographical scales of analysis (Fisher, Whittaker, & Malhi, 2011).

Evapotranspiration mapping across complex hydro-climatic conditions proves challenging due to the difficulty of solving the energy balance equations and the required model parameters because of increased uncertainty with input data and model structures, particularly across scene boundaries. Thus, to meet the needs of a basin-wide estimate, Senay et al. (2013) introduced a novel empirical parameterization to an existing simplified modeling approach (Senay et al., 2007) to produce a seamless ET across image-scenes using the Operational Simplified Surface Energy Balance (SSEBop) approach. A comprehensive validation of SSEBop ET estimates over the conterminous United States was performed using 60 FLUXNET station datasets (Velpuri, Senay, Singh, Bohms, & Verdin, 2013). Singh, Senay, Velpuri, Bohms, Scott, et al. (2014) and Singh, Senay, Velpuri, Bohms & Verdin (2014) created the first-ever basin-wide monthly and annual ET for 2010 for the entire Colorado River Basin (CRB) at the Landsat spatial scale using the SSEBop model.

One of the challenges of working with Landsat imagery is the large number of images required to cover an entire basin. For example, the CRB requires 43 Landsat scenes (path/row) each with a nominal area of about 180 km × 170 km. To obtain an annual ET estimate, each path/row has a potential of 22 images per year (assuming a single functional Landsat with a 16-day repeat cycle). Due to cloud cover, some of these 22 images may not be usable. This creates a differential number of usable images from year to year forcing the annual estimation to rely on interpolation techniques for the missing images.

The main objectives of the study are to (1) use Landsat 8 images to produce annual ET for the entire Colorado River Basin for 2013, (2) evaluate the performance of Landsat 8-derived ET using independent datasets such as eddy covariance (EC) and water balance ET approaches, and (3) assess the opportunities and challenges in using Landsat 8 for estimating basin-wide crop consumptive use towards meeting the USGS National Water Census objectives.

## 2. Data

We used various datasets from different sources ranging from field measurements to remotely sensed images for the Colorado River Basin (Fig. 1). A list of all datasets used in this study and their characteristics are provided in Table 1.

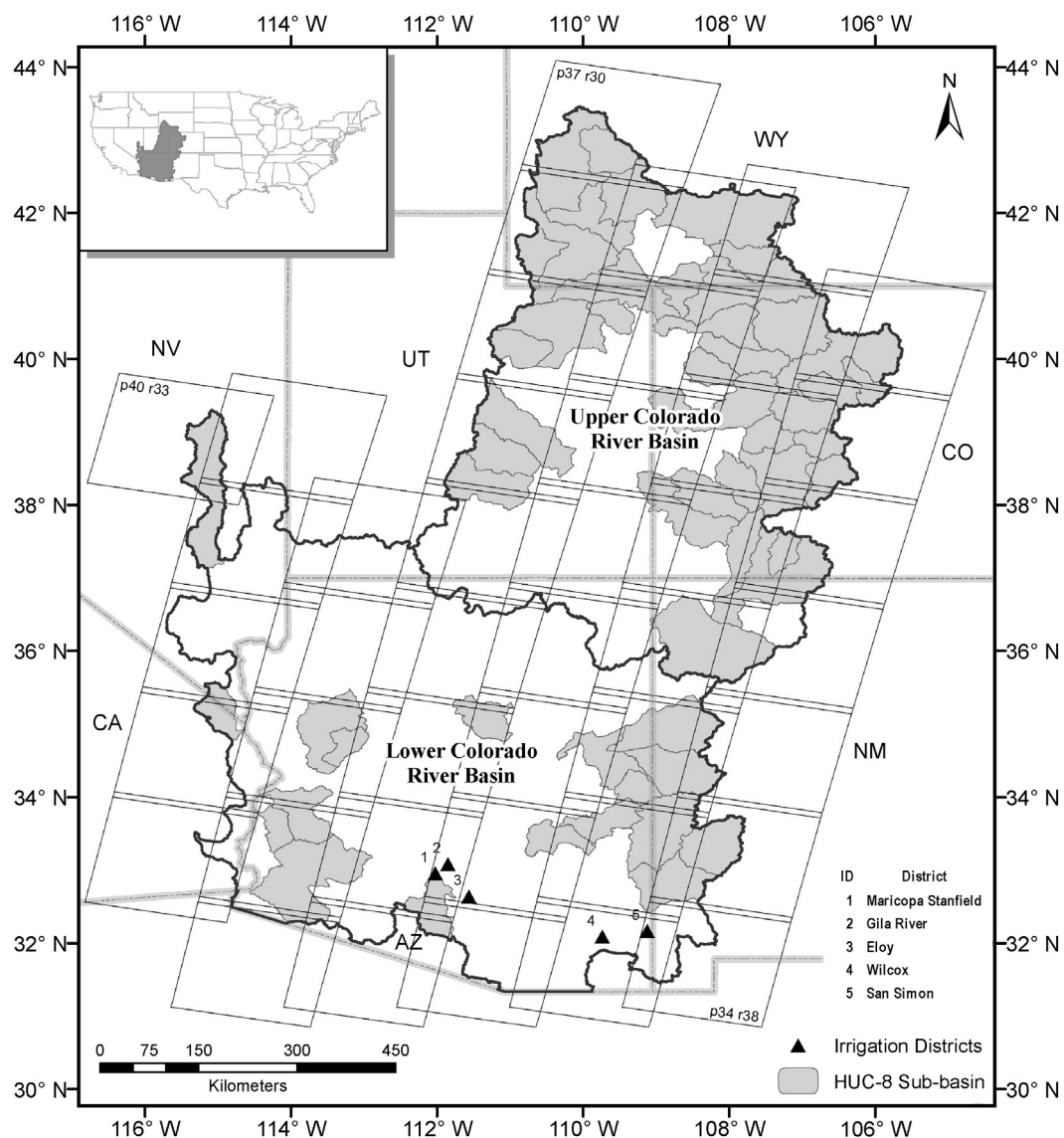


**Fig. 1.** Location map of the study area, the Colorado River Basin in the United States, with boundaries of U.S. states. The footprint of Landsat 8 based on Worldwide Reference System-2 for each path/row is also shown and labeled for top, bottom right, and extreme left scenes. The location of the five irrigation districts and selected sub-basins (hydrologic unit code 8) for water balance ET validation are also shown.

## 2.1. Input datasets

We downloaded 528 Landsat 8 images (Irons et al., 2012) covering the CRB (Paths 33–40, Rows 30–38) that had cloud cover less than 60%. The number of images used for each scene varied from 15 (path/row 37/32, 37/34, 35/38, 35/35) to 9 (path/row 36/35, 37/37). The number of days between usable images also varied as some areas had more cloud cover than others. Thermal band 10 was used to compute land surface temperature ( $T_s$ ), and the Normalized Difference Vegetation Index (NDVI) was computed from red and near-infrared bands. The reference daily evapotranspiration ( $E_{to}$ ) product was produced using 6-hourly meteorological data from the National Oceanic and Atmospheric Administration (NOAA) Global Data Assimilation System (GDAS) using the standardized Penman–Monteith equation (Senay, Verdin, Lietzow, & Melesse, 2008). The coarse (100 km) GDAS  $E_{to}$  was downscaled to a 10 km spatial resolution using higher spatial resolution climatologic  $E_{to}$  according to Senay et al. (2007). Validation of the GDAS  $E_{to}$  using  $E_{to}$  derived from the weather station observations from the California Irrigation Management Information System (CIMIS) revealed a high correlation coefficient of 0.99 (Senay et al., 2008). Gridded air

temperature at 1-km spatial resolution for the CRB region was obtained from the Daymet database. Daymet is a collection of gridded estimates of daily weather parameters generated by interpolation and extrapolation from daily meteorological observations (Thornton et al., 2014). The albedo data used in this study are obtained from the MODIS Terra/Aqua albedo product (MCD43B3). The MODIS albedo dataset algorithm is derived from multiday, cloud-free, atmospherically corrected surface reflectance observations collected by the first seven land bands in the Visible and Near-infrared (VNIR) spectrum (Schaaf et al., 2002). Shuttle Radar Topography Mission (SRTM) topographic elevation data at 30-m spatial resolution were obtained from the USGS (Farr & Kobrick, 2000).

## 2.2. Validation datasets

In this study, we used two different validation approaches: 1) point-scale validation and 2) basin-scale validation.

### 2.2.1. Point-scale validation datasets

For the point-scale validation, we used eddy covariance FLUXNET (Baldocchi et al., 2001) data from two sites: Santa Rita mesquite and

**Table 1**  
List and characteristics of data used in this study.

No	Source/satellite/sensor	Parameter	Frequency	Resolution	Reference
1	Landsat 8 (TIRS, VNIR)	Land surface temp ( $T_s$ ) and NDVI	Monthly (04–12/2013)	100 m	Irons, Dwyer, and Barsi (2012)
2	Daymet	Max air temp ( $T_a$ ) Avg. net radiation ( $R_n$ )	Daily 2013	1000 m	Thornton et al. (2014)
3	SRTM	Elevation, $Z$	–	30 m	Farr and Kobrick (2000)
4	GDAS	Reference $E_{to}$	Daily climatology (0–12)	10,000 m	Senay et al. (2007)
5	MODIS (MCD43B3)	Albedo, $\alpha$	16 day climatology (0–12)	1000 m	Schaaf et al. (2002)
6	Eddy covariance	$LE$ , $G$ , $H$	Monthly (2013)	–	Baldocchi et al. (2001)
7	PRISM precipitation	Precipitation, $P$	Monthly (2013)	4000 m	Daly et al. (2000)
8	Stream gage stations	Streamflow, $Q$	Monthly (2013)	–	Jian, Wolock, and Lins (2008)
9	USGS hydrologic units	HUC8 boundaries	–	–	Seaber, Kapinos, and Knapp (1987)
10	NASS, USDA	Crop type	Annual (2013)	30 m	Boryan, Yang, Mueller, and Craig (2011)
11	NLCD, 2011	Land cover	Annual (2011)	30 m	Jin et al. (2013)

TIRS: Thermal Infrared Sensor, VNIR: Visible and Near-infrared, NDVI: Normalized Difference Vegetation Index, SRTM: Shuttle Radar Topography Mission, GDAS: Global Data Assimilation System, MODIS: Moderate Resolution Imaging Spectroradiometer,  $LE$ : latent heat flux,  $G$ : soil heat flux,  $H$ : sensible heat flux, PRISM: Parameter-elevation Regressions on Independent Slopes Model, HUC: hydrologic unit code, NASS: National Agricultural Statistical Service, USDA: U.S. Department of Agriculture, and NLCD: National Land Cover Database.

Kendall grassland. The Santa Rita mesquite site is located at 31.8214 °N, 110.8661 °W (elevation: 1116 m above mean sea level) about 45 km south of Tucson, Arizona, in a semi-desert grassland. The mean annual (1937–2007) precipitation at this site is 377 mm. The vegetation at this site consists of native grasses (*Digitaria californica*, *Muhlenbergia porteri*, *Bouteloua eriopoda*, and *Aristida* spp.), nonnative perennial  $C_4$  grasses (mainly *Eragrostis lehmanniana* Nees), shrubs (mainly *Isocoma tenuisecta* Greene), and scattered succulents (*Opuntia* spp.). Fluxes were measured using a three-dimensional, sonic anemometer (CSAT-3, Campbell Scientific), and an open-path infrared gas analyzer (LI-7500, LI-COR). The data were sampled at 10 Hz and recorded by a data logger (CR5000, Campbell Scientific). In general, the energy balance closure error at this site is about 14% on a half hourly basis and about 8% on a daily basis (Scott, 2010), which is within the normal range of energy balance closure obtained by the eddy covariance measurements (Wilson et al., 2002). More details about this EC site can be obtained from Scott, Jenerette, Potts, and Huxman (2009) and Scott (2010).

The Kendall grassland site is located at 31.7365 °N, 109.9419 °W (elevation: 1530 m above mean sea level) in the upper end of the U.S. Department of Agriculture (USDA) Walnut Gulch Experimental Watershed at Tombstone, Arizona, with a mean annual (1964–2009) precipitation of 345 mm. The vegetation at this site comprises mainly of  $C_4$  grasses (*B. eriopoda*, *B. hirsuta*, *Hilaria belangeri*, and *Aristida hamulosa*) interspersed with  $C_3$  shrubs (*Calliandra eriophylla*, *Dalea formosam*, *Krameria parvifolia*, *Prosopis glandulosa*, *Yucca elata*, and *I. tenuisecta*). Fluxes were measured using a three-dimensional, sonic anemometer (CSAT-3, Campbell Scientific), and an open-path infrared gas analyzer (LI-7500, LI-COR) mounted at a height of 6.4 m. The data were sampled at 10 Hz and recorded by the data logger (CR5000, Campbell Scientific). In general, the energy balance closure error at this site was far from ideal but the ratio of the sum of latent and sensible heat fluxes to available energy was near unity on an annual basis (Scott, Hamerlynck, Jenerette, Moran, & Barron-Gafford, 2010). Additional details about this EC site can be obtained from Scott (2010) and Scott et al. (2010).

### 2.2.2. Basin-scale validation datasets

Basin-scale validation was performed at hydrologic unit code (HUC) 8 sub-basins. The entire United States is divided into different levels of hydrologic units that are identified by a unique hydrologic unit code number (Seaber et al., 1987). The hydrologic unit code represents two digits each to indicate region (HUC2), sub-region (HUC4), basin (HUC6), and sub-basin (HUC8). The HUC-based classification system is generally used by federal and state agencies as the basis for reporting and planning water use and development. In this study, we performed basin-scale comparisons of Landsat 8 based ET (L8ET) summarized by HUC8 sub-basins. The CRB is divided into 140 HUC8 sub-basins with an average surface area of 4500 km<sup>2</sup>. Monthly and annual total

precipitation ( $P$ ) for 2013 for each HUC were summarized from gridded 4-km monthly Parameter-elevation Regressions on Independent Slopes Model (PRISM) precipitation datasets (Daly, Smith, Smith, & McKane, 2007; Daly et al., 2000) obtained from the PRISM Climate Group website (<http://www.prism.oregonstate.edu/>). PRISM products are the official climatological datasets of the U.S. Department of Agriculture and are considered to be the highest quality spatial climate datasets for the United States (Di Luzio, Johnson, Daly, Eischeid, & Arnold, 2008). Additionally, monthly 4-km runoff estimates from different HUC8 sub-basins for the CRB were obtained from the USGS WaterWatch website (<http://waterwatch.usgs.gov/>). Estimates of monthly runoff data for each HUC8 are generated by combining the USGS flow data from stream gages, drainage basins of stream gages, and basin boundaries (Jian et al., 2008). Since runoff data were only available through September 2013, long-term mean runoff (1950–2013) for October–December months was computed and combined with 2013 data to estimate annual runoff for each HUC8 sub-basin.

In order to understand monthly change in water storage for each HUC8 sub-basin, we used Gravity Recovery and Climate Experiment (GRACE) monthly mass deviation data (MD). We also used RL05 1° × 1° mass grids generated by National Aeronautics and Space Administration (NASA) Jet Propulsion Laboratory obtained from the GRACE Tellus website (<http://grace.jpl.nasa.gov/data/gracemonthlymassgridsland/>). Land-grid scaling coefficients were applied to minimize the difference between the smoothed (modeled) and unfiltered monthly water storage variations. Measurement and leakage errors in the RL05 product were aggregated for each HUC8 sub-basin (Landerer & Swenson, 2012). To minimize errors, monthly variations in GRACE MD were summarized by computing spatial averages for all the HUC8 sub-basins within the CRB. Finally, monthly and annual changes in storage were computed as suggested by Senay, Velpuri, Bohms, Demissie, and Gebremichael (2014). Annual PRISM rainfall estimates, annual runoff data, and annual change in storage for each HUC8 sub-basin were used to estimate HUC8-level water balance ET.

### 2.3. Other ancillary datasets

National Agricultural Statistical Service (NASS) of the U.S. Department of Agriculture (USDA) has produced the Cropland Data Layer (CDL) for the conterminous United States annually since 2008 (Boryan et al., 2011). The CDL is a georeferenced 30-m raster layer that provides information on crop-specific land cover data and classification. We used the 2013 CDL dataset to extract crop type information for various irrigation districts in the Lower CRB. Irrigation district boundaries for five locations (Fig. 1) were obtained from the USGS Arizona Water Science Center. We also used National Land Cover Database (NLCD) 2011 (Jin et al., 2013) to summarize evapotranspiration by 16 land cover classes within the CRB. NLCD 2011 is the most recent national land cover

product (with 30 m resolution) created by the Multi-Resolution Land Characteristics (MRLC) Consortium.

### 3. Methodology

#### 3.1. The SSEBop modeling approach

The SSEBop model does not solve all the energy balance terms explicitly; rather, it defines the limiting conditions based on clear-sky net radiation balance principles. The SSEBop approach (Senay et al., 2013) predefines unique sets of “hot/dry” and “cold/wet” limiting values for each pixel unlike the original SSEB formulation, which uses a set of reference hot and cold pixel-pairs applicable for a limited, uniform hydro-climatic region. To estimate ET routinely, the only data needed for the SSEBop method are surface temperature ( $T_s$ , K), air temperature ( $T_a$ , K), and a potential ET, represented by a preferred reference crop type and adjusted by a scaling factor. In this case we used the grass reference ET ( $ET_o$ , mm).

With this simplification, actual ET ( $ET_a$ ) can be estimated using Eq. (1) as a fraction of the  $ET_o$ .

$$ET_a = ET_f * k * ET_o \quad (1)$$

where  $ET_o$  is the grass reference ET for the location;  $k$  is a coefficient that scales the  $ET_o$  into the level of a maximum ET experienced by an aerodynamically rougher crop such as alfalfa. For the current SSEBop model parameterization, a recommended value for  $k$  equal to 1.0 was used in this study (Senay et al., 2013; Singh, Senay, Velpuri, Bohms, Scott, et al., 2014).

The ET fraction ( $ET_f$ ) is calculated using Eq. (2):

$$ET_f = \frac{Th - Ts}{dT} = \frac{Th - Ts}{Th - Tc} \quad (2)$$

where  $T_s$  is the satellite-observed land surface temperature of the pixel whose  $ET_f$  is being evaluated on a given image date;  $Th$  is the estimated  $T_s$  at the idealized reference “hot/dry” limit of the same pixel for the same time period;  $Tc$  is the estimated  $T_s$  at the idealized “cold/wet” limit of the same pixel; and  $dT$  is a predefined temperature difference between  $Th$  and  $Tc$  for each pixel. Negative  $ET_f$  is set to zero and maximum  $ET_f$  is capped at 1.05 or to “no data” for cloudy pixels.

The cold limiting condition,  $Tc$ , is calculated from  $Ta$  as follows. Because the Landsat satellite thermal data ( $T_s$ ) are acquired during the morning hours at a nominal overpass time of 10:30 am,  $T_s$  is more closely related to daily maximum air temperature than to the daily minimum temperature. The daily maximum air temperature is more readily available than the hourly temperature from weather datasets for large-scale applications. After examining the relationship between  $T_s$  and Daymet data (Thornton et al., 2014) daily maximum air temperature ( $T_{max}$ ) in well-vegetated pixels, where NDVI is greater than 0.8, a median correction coefficient of 0.985 ( $Tc = 0.985 * T_{max}$ ) was established from Landsat images acquired throughout the CRB (Singh, Senay, Velpuri, Bohms, Scott, et al., 2014). Senay et al. (2013) report details on the procedure used for establishing the correction coefficient,  $c$ . Then  $Th$  is computed as the sum of  $Tc$  and  $dT$ . The overall approach of the SSEBop model is presented in Fig. 2.

In this case,  $dT$  is predefined for each pixel as explained in Senay et al. (2013) using Eq. (3). The variable,  $dT$ , is calculated under clear-sky conditions and assumed not to change from year to year, but is unique for each day and location.

$$dT = \frac{Rn * r_{ah}}{\rho_a * C_p} \quad (3)$$

where  $Rn$  is daily average clear-sky net radiation  $J \cdot m^{-2} \cdot s^{-1}$  (calculated using Daymet data),  $r_{ah}$  is the aerodynamic resistance to heat transfer from a hypothetical bare and dry surface, taken as  $110 s \cdot m^{-1}$  (Senay et al., 2013).  $\rho_a$  is the density of air ( $kg/m^3$ ), estimated as a function of air pressure and temperature (Allen, Pereira, Raes, & Smith, 1998); and  $C_p$  is the specific heat of air at constant pressure ( $1.013 kJ \cdot kg^{-1} \cdot K^{-1}$ ). All are taken with multiplying factors for consistent energy, mass, volume, and time units.

With an algebraic rearrangement of Eqs. (1) to (3),  $ET_a$  can be formulated as the product of commonly used surface energy balance parameters as shown in Eq. (4).

$$ET_a = \frac{\rho_a * C_p}{Rn * r_{ah}} (Th - Ts) * k * ET_o \quad (4)$$

The most important simplification is based on the knowledge that the surface energy balance process is mainly driven by the available net radiation ( $Rn$ ). Since thermal remote sensing is mainly used under clear-sky conditions, the SSEBop method assumes a location- and date-specific constant temperature difference ( $dT$ , K) between the hot/dry and cold/wet limiting reference points. While converting the daily average net radiation into sensible heat at the time of satellite-overpass, we realize the temporal mismatch between the instantaneous satellite-overpass and the daily average net-radiation. As empirical data show (Section 4.4), the daily average clear-sky net radiation is a good predictor of the available cumulative energy that would raise the temperature of a bare-dry surface at the time of satellite overpass, with a seasonal range of 2 to 25 K on winter and summer days, respectively. This not only assumes clear-sky at the time of satellite overpass but also clear-sky for the entire day. However, this assumption is only used to get an empirical estimate of  $dT$  but not to solve the energy balance at the time of satellite overpass and hence the approach appears to hold as a good estimator of  $dT$ , removing the need to manually select hot and cold pixels.

#### 3.2. Landsat 8 data processing

We used the approach for processing Landsat images as provided in Singh, Senay, Velpuri, Bohms, Scott, et al. (2014) and Singh, Senay, Velpuri, Bohms & Verdin (2014). The digital number (DN) values were first converted to radiance and then to reflectance. The land surface temperature ( $T_s$ ) values were derived from Landsat 8 thermal data, specifically Thermal Infrared Sensor (TIRS) band 10. For this purpose, the SSEBop approach incorporated a set of algorithms composed of commonly used calibration steps and atmospheric correction techniques. These included calculation steps for: (1) spectral radiance conversion to the at-sensor brightness temperature; (2) atmospheric absorption and re-emission value; (3) surface emissivity; and (4) land surface temperature. The  $T_s$  values were computed using a modified equation (Allen et al., 2007) with both atmospheric and surface emissivity calculations as:

$$T_s = \frac{K_2}{\ln\left(\frac{\epsilon_{NB} * K_1}{R_c} + 1\right)} \quad (5)$$

where,  $K_1$  and  $K_2$  are prelaunch calibration constants;  $\epsilon_{NB}$  is the narrow band emissivity derived from a modification of the NDVI thresholds method (Sobrino, Jiménez-Muñoz, & Paolini, 2004); and  $R_c$  is the corrected thermal radiance using mean values for path radiance, narrow band downward thermal radiation, and narrow band transmissivity of air (Wukelic, Gibbons, Martucci, & Foote, 1989). Emissivity values were computed using the NDVI-based algorithm (Sobrino et al., 2004). Corrected thermal radiance ( $R_c$ ) is derived using an algorithm given by Wukelic et al. (1989) using assumptions reported in Allen et al. (2007). Because the modeling approach evaluates the  $T_s$  as a relative

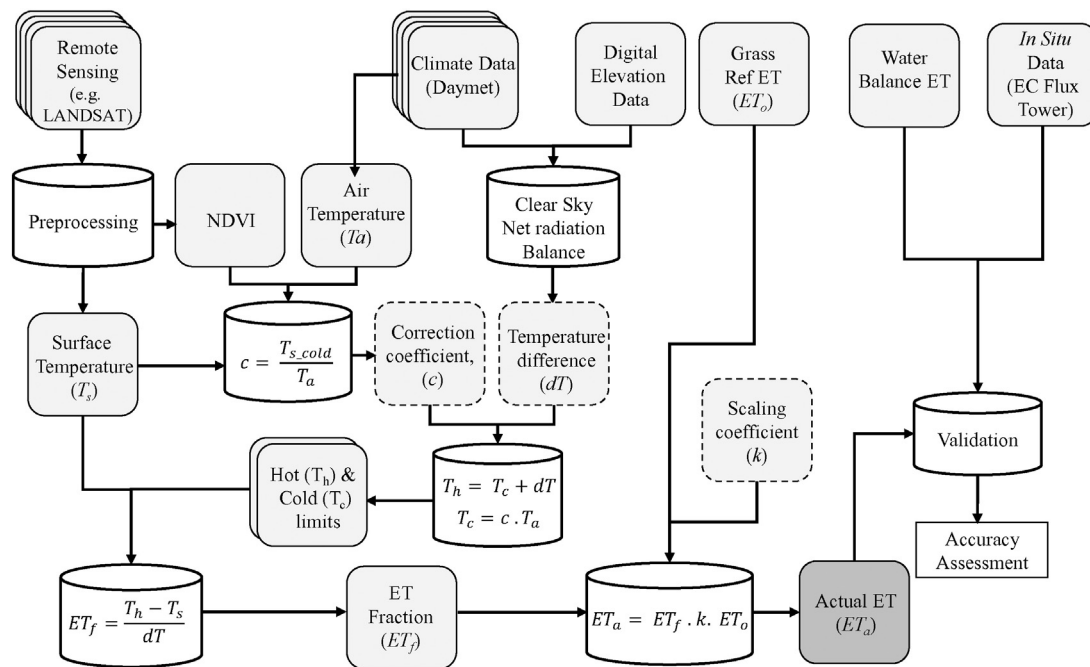


Fig. 2. Overview of the SSBop model methodology.

ET fraction between the hot/dry and cold/wet limiting values, the consistency of Eq. (5) across space and time is more important than getting the absolute magnitude correct.

### 3.3. Cloud masking and gap filling

Automated cloud screening has increasingly allowed scientists to create more value-added products that can be used confidently for land surface characterization studies. While selecting consistent and accurate techniques can be a subjective and time-consuming endeavor, a number of cloud detection algorithms have been evaluated and integrated within the Landsat community for multiple sensors (Huang et al., 2010; Irish, Barker, Goward, & Arvidson, 2006; Roy et al., 2010; Zhu & Woodcock, 2012). The Fmask (Function of mask) algorithm is designed to concurrently detect cloud, cloud shadow, and snow at the same time (Zhu & Woodcock, 2012).

Recently, the USGS EROS Center integrated the cloud mask algorithm CFmask (C version of the Fmask) into the Landsat surface reflectance Climate Data Record (CDR) (Maiersperger et al., 2013; Masek et al., 2006). Additionally, the Landsat 8 infrared channel for cirrus cloud detection, band 9 (1.36–1.38  $\mu\text{m}$ ), has been incorporated into the Fmask algorithm for improved cloud detection results (Zhu & Woodcock, 2012). The addition of this specific band is especially helpful for detecting high altitude clouds, especially cirrus clouds. Because of these spectral additions and enhanced cloud-masking capability of Landsat 8 for the improved removal of contaminated pixels, we opted to use the Fmask version 3.2 algorithm to effectively create cloud and shadow masks for our processing environment (Zhu & Woodcock, 2012).

We followed an integrated approach for Landsat cloud detection and fill processes in an automated ET modeling environment. Identifying contaminated or cloudy pixels is an essential first step in the process of attempting to fill images containing cloudy pixels. A gap-filled product yields improved visual and analytical results not just at the overpass time, but also at monthly and annual levels. We retained the spatial integrity of Landsat 8 data while preserving relative magnitude in model estimation by incorporating a pixel-by-pixel ET fraction gap filling. This technique included a standard linear interpolation approach

using adjacent cloud-free pixels through an iterative, multi-step process for each image in a given path and row.

The relative values of interpolated pixels (for a cloudy location) between two or more cloud-free scenes with valid model estimates can provide important derivative data for spatial context in a “gap-filling” sense, while allowing for assessment of magnitude and accuracy among overpass, monthly, and annual estimates. With the 16-day revisit cycle of Landsat 8, we inevitably approached scenarios of one (or more) cloudy observation after another in a given pixel location. As a result, on occasions where interpolation proved insufficient (or unwarranted) over repeatedly masked pixels, instead of referencing a default fill-value we turned to inspection of a scene-constrained limiting ratio between overpass Landsat  $ET_f$  and its nearest Moderate Resolution Imaging Spectroradiometer (MODIS)  $ET_f$  to fill remaining voids. For this last step, we implemented the scaled relationship of a median (2000–2012) MODIS  $ET_f$  (8-day) pixel with that of Landsat  $ET_f$  (overpass), assuming scene-wide relative ratio uniformity.

This step addresses any biases or limitations of a scene-wide ratio approach across derivative datasets with differing resolutions (Landsat: 100 m, MODIS: 1000 m). Furthermore, integration of MODIS  $ET_f$  in this manner is retained as a secondary fill step, as assigned beyond the iterative, linear interpolation of available Landsat data. Subsequently, the observed visual and analytical impacts on annual ET in this study were minimal, with just an estimated 2–3% visible fill-effect over persistently masked terrain in parts of the Upper CRB.

### 3.4. Monthly aggregation

Due to the temporal nature of Landsat data acquisition, monthly aggregation is required for computing monthly and annual ET estimates from the day of satellite overpasses. As indicated earlier, our modeling efforts initially calculated actual daily ET ( $ET_a$ ) values for each overpass scene using daily gridded  $ET_0$  and an  $ET_f$  created from Landsat 8. The annual ET product is based on a monthly cumulative approach. To create a monthly ET product, actual ET was estimated for a period of aggregation (e.g., monthly) defined by the reference ET. Annual ET is then obtained by simple summation. We automated this summation calculation

through multiple steps in order to quickly represent the accurate combination of overpass  $ET_f$  and daily  $ET_o$ . In essence, the daily  $ET_a$  values for dates between images were derived by the daily  $ET_o$  and its nearest respective overpass  $ET_f$ . This allowed the reference ET dataset to capture the general ET trend over the course of a month, season, and year, while incorporating modeled  $ET_f$  from Landsat results for accurate actual ET estimates. Additional details on aggregating monthly and seasonal ET from temporal satellite images are provided in Singh, Liu, Tieszen, Suyker, and Verma (2011).

This study has shown promising spatiotemporal results using Landsat 8 images ranging from 9 to 15 images per scene. The monthly ET for the months prior to launch of Landsat 8 satellite was estimated based on  $ET_o$  and  $ET_f$  values from the first available image. However, this may not have any major impact on the annual ET as the amount of water lost through ET is minimal during those early winter months when considered over larger landscapes in the basin.

### 3.5. Basin-scale validation using water balance ET (WBET)

The application of the water balance approach for ET estimation has been limited over regional or basin scales mainly due to inaccuracies in precipitation and runoff and the inability to close the water balance due to non-availability of storage information or an invalid assumption of negligible storage ( $\Delta S \neq 0$ ) at monthly or annual time scales. In this study, Landsat 8-based ET estimates were validated using water balance ET (WBET). WBET has been widely used to validate remote sensing-based ET at a regional or watershed scale (Senay et al., 2011; Velpuri et al., 2013; Zhang, Kimball, Nemani, & Running, 2010). Following the basic water balance calculation procedures, WBET can be estimated for each HUC8 sub-basin as

$$WBET = P - Q - \Delta S \quad (6)$$

where  $P$ ,  $Q$ , and  $\Delta S$  are annual basin precipitation, basin runoff, and change in storage, respectively. Using HUC8 boundary information, we computed annual estimates of WBET to validate annual ET from Landsat 8. Since this approach is based on water balance, we excluded HUC8 sub-basins where water balance was not expected to close ( $WBET \neq P - Q - \Delta S$ ) due to the factors listed below. First, we excluded data from sub-basins where the runoff–rainfall coefficient ( $Q/P$ ) is more than 0.55 (Velpuri et al., 2013). This condition enabled us to ignore sub-basins that have dominant regional groundwater flow, which could introduce error in the WBET estimates. Second, we excluded HUC8 sub-basins with negative WBET values (where combined  $(Q + \Delta S) > P$ ). Third, to enable comparison of similar sub-basins, we excluded those where Landsat 8 ET was more than  $P$ . This exclusion was mainly because SSEBop provides ET estimates from all land cover types (including water bodies); HUC8s with large permanent water bodies will have high ET values that cannot be accounted for by precipitation alone. Furthermore, sub-basins with large irrigation districts would also result in higher ET values that could not be accounted for by WBET.

## 4. Results and discussion

### 4.1. Actual evapotranspiration map of the Colorado River Basin

The actual evapotranspiration map of the Colorado River Basin shows the spatial variation of annual ET for 2013 (Fig. 3). Based on this ET map, annual ET in the CRB varied widely from low values in the barren lands to high values over open water bodies and irrigated cropland. In general, ET varies depending upon land use/land cover, vegetation growth and stages, climate, soil moisture availability, and management practices. Some of the highest ET from cropland areas is located in the Lower Colorado River Basin, indicating intensive agricultural practices. As expected, water bodies had the maximum annual

ET among all the land use/land cover classes summarized using NLCD 2011 data (Table 2). It should be noted that open-water ET estimates has higher uncertainty as the SSEBop model result does not account for additional energy sources such as water body heat storage or differences in optical properties of water bodies. Cropland had the next highest mean annual ET of 726 mm with a spatial standard deviation (SD) of 372 mm. Because shrubland is the most pervasive land cover within the CRB, it consumed the highest volume of water, at 146 km<sup>3</sup>/year (14.6 million ha-m/year) followed by evergreen forest (78 km<sup>3</sup>) and grasslands (17 km<sup>3</sup>) (Table 2). In comparison, the consumptive use of cropland was only about 4.15 km<sup>3</sup>/year (0.42 million ha-m/year) with much of this derived from irrigation. Thus, croplands consumed the largest amount of blue water (managed surface and ground water) and shrublands consumed the most green water (natural rainfall and soil moisture) sources. The ranking of annual ET for different land use/land cover classes for 2013 was comparable to the ranking found for 2010 as reported in (Singh, Senay, Velpuri, Bohms, Scott, et al., 2014). There were differences in absolute magnitude of annual ET between 2010 and 2013, which may be attributed to differences in the total number and timing of Landsat images used in these studies and differences in image selection criteria. A total of 328 cloud-free (<10% cloud) Landsat images were used for the 2010 study, whereas 528 Landsat 8 images (<60% clouds) were used in this study. The earliest Landsat 8 image used for 2013 ET estimates within the CRB was acquired on 13 April 2013, whereas images from Landsat 5 and 7 were used starting in January 2010. However, a separate analysis (not shown) suggests that the extrapolation of the early winter months from the spring season images using reference ET was adequate because of the small contribution coming from the early months. This aspect is further discussed in Section 4.5.

### 4.2. SSEBop model validation using flux tower data

We found good correlation ( $r = 0.91$ – $0.95$ ) between the eddy covariance measured ET and the SSEBop modeled ET at two flux towers (Table 3). The mean absolute errors (MAE) were 0.35 mm d<sup>-1</sup> and 0.39 mm d<sup>-1</sup> on the days of satellite overpasses and 9.89 mm month<sup>-1</sup> and 7.03 mm month<sup>-1</sup> on a monthly basis at the Santa Rita mesquite and Kendall grassland sites, respectively. There was a good match between the observed and the estimated ET at the Kendall grassland sites both on a daily ( $y = 0.9992x$ ,  $R^2 = 0.82$ ) and monthly ( $y = 1.0001x$ ,  $R^2 = 0.91$ ) basis (Fig. 4). Overall, the SSEBop model overestimated ET at the Kendall grassland site by about 13% on the days of satellite overpass and only by about 2% on a monthly basis with Nash–Sutcliffe coefficient of efficiency (NSCE) values of 0.80 and 0.91, respectively. Better performance of the SSEBop model at the Kendall grassland site can be attributed to temporal variation of  $T_s$  within the hot/dry and cold/wet limiting conditions (Fig. 5), resulting into calculation of  $ET_f$  value instead of a no data point.

We found good correlation ( $r = 0.91$ ,  $R^2 = 0.82$ ) between measured and estimated ET at the Santa Rita mesquite site for the days of satellite overpasses. However, contrary to the Kendall grassland site, the SSEBop model underestimated ET at the Santa Rita mesquite site by about 22% on a daily basis and by about 35% on a monthly basis with Nash–Sutcliffe coefficient of efficiency values of 0.75 and 0.67, respectively. Relatively increased monthly bias at this site can be attributed to availability of the first usable Landsat 8 image only on 11 June 2013 and cloud contamination on two dates (day of year: DOY 194 and 242) when the  $T_s$  was much lower than  $T_c$  (Fig. 5a). Furthermore, such examples allowed us to evaluate the successes and limitations of our pixel-fill  $ET_f$  interpolation method against validation site data (Fig. 5b). We have provided additional discussion on this aspect and the Fmask algorithm in Section 4.5. Ideally, all  $T_s$  values should be within the two limiting conditions,  $T_c$  and  $T_h$ . Whenever this assumption is violated, ET will be set to zero for the lower limit or filled in by adjacent periods for cloudy pixels. Singh, Senay, Velpuri, Bohms & Verdin (2014) used Landsat

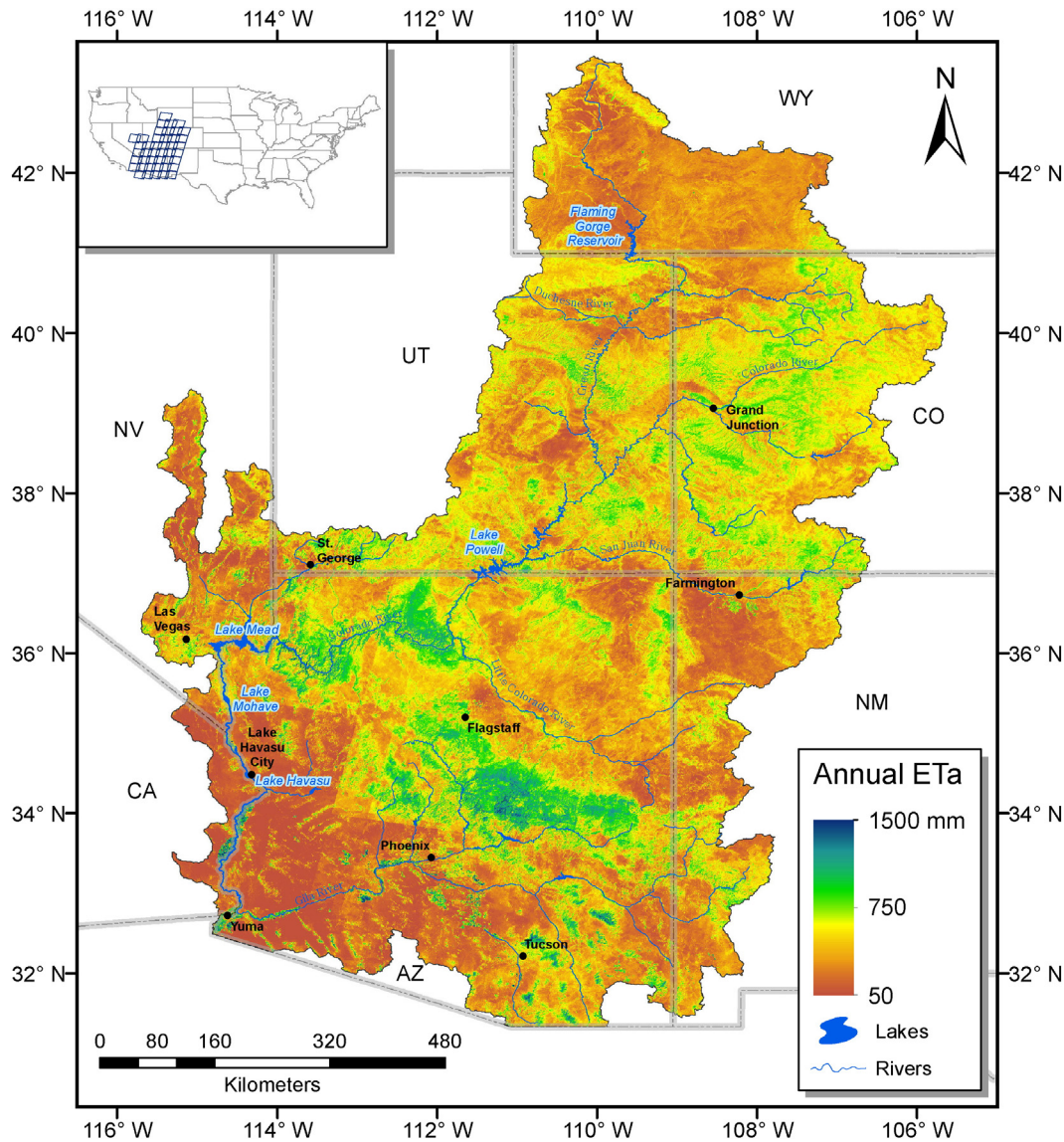


Fig. 3. Spatial distribution of the annual evapotranspiration (mm) for 2013 using the SSEBop model based on Landsat 8 and other ancillary data.

and MODIS images for 2010 and found a lower bias at the Santa Rita mesquite site (mean bias = -2 mm, root mean square error (RMSE) = 12 mm,  $R^2 = 0.72$ ) and at the Kendall grassland site (mean

bias = -9 mm, RMSE = 13 mm,  $R^2 = 0.81$ ). This difference in performance was most likely due to use of the combination of Landsat and MODIS images in computing monthly ET for 2010.

Table 2

Total area, mean annual evapotranspiration, standard deviation, and total annual ET for different land use/land cover classes within the Colorado River Basin during 2013.

LC Code	Land cover	Area (km <sup>2</sup> )	2013 mean annual ET (mm/year)	2013 SD (mm/year)	2013 total annual ET (km <sup>3</sup> /year)
11	Water	2518	1223	495	3.08
82	Cropland	5723	726	372	4.15
43	Mixed forest	2141	708	124	1.52
41	Deciduous forest	20,450	676	128	13.82
90	Woody wetland	3258	670	263	2.18
42	Evergreen forest	117,030	669	206	78.29
81	Pasture hay	7332	601	253	4.41
95	Emergent herb. wetland	1115	518	293	0.58
12	Ice/snow cover	297	502	84	0.15
22	Low intensity developed	3191	469	228	1.50
24	High intensity developed	502	458	220	0.23
23	Medium intensity developed	1925	457	211	0.88
31	Barren	21,103	434	249	9.16
21	Open space developed	4992	431	245	2.15
52	Shrubland	397,143	368	211	146.15
71	Grassland	45,803	364	173	16.67

**Table 3**  
Comparison statistics for eddy covariance measurement and Landsat 8 evapotranspiration based on the SSEBop model.

Statistic	Santa Rita mesquite		Kendall Grassland	
	Daily	Monthly	Daily	Monthly
N	12	12	15	12
Observed mean (mm)	1.24	27.93	0.93	26.37
r	0.91	0.92	0.91	0.95
R <sup>2</sup>	0.82	0.85	0.82	0.91
MAE (mm)	0.35	9.89	0.39	7.03
RMSE (mm)	0.60	13.04	0.48	7.75
NSCE	0.75	0.67	0.8	0.91
Relative bias (%)	-22.13	-34.66	13.06	2.4
Standard error (mm)	0.43	8.68	0.49	8.43

4.3. Basin-scale validation using water balance ET (WBET)

Basin-scale validation results using water balance ET (WBET) are presented in Fig. 6. Compared to the WBET, Landsat 8 ET shows a reasonable R<sup>2</sup> value of 0.78. The RMSE was found to be 77 mm year<sup>-1</sup> with a relative bias of 7%. In order to understand the accuracies better, we summarized the results for the Upper and the Lower Colorado River Basins separately. Accuracy of the Lower CRB was found to be slightly better than the Upper CRB because selected HUC8 sub-basins in the Lower CRB are semiarid to arid where most of the ET is precipitation based. In contrast, the Upper CRB has several (a) scattered irrigation projects (both surface and groundwater fed), (b) mountain forests (that tap groundwater) and (c) surface storage structures that also contribute to ET. Actual estimates of R<sup>2</sup>, RMSE, and bias for both the Lower and Upper CRB are summarized in Fig. 6.

4.4. Benefits of Landsat in water resources

There are many uses and benefits of Landsat images for water resource applications (Serbina & Miller, 2014). The results of this study show that field-scale management practices can be carried out using Landsat images because the spatial resolution allows field characterization of ET. Fig. 7 shows the distribution of irrigated fields in the Southern Willcox irrigation district, where cotton is the dominant crop. Total annual water use of individual fields is captured by the SSEBop model using Landsat 8 images as shown in Fig. 7a. To understand the variability of annual water use for a specific crop, we overlaid field boundaries of alfalfa cropland obtained from 2013 CDL. Low ET over a few alfalfa fields

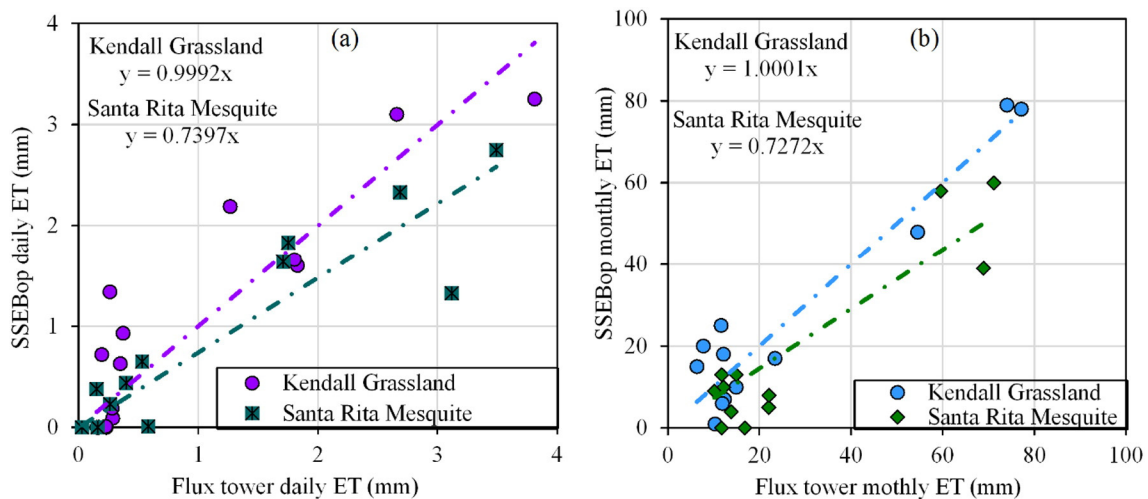
is most likely due to the inaccuracies (commission errors) in CDL classification. A high degree of variability in annual water use can be observed for the alfalfa crop. This variability suggests the presence of different land and water management practices for a similar crop. Irrigation district managers could use such annual water use information for determining allocation of water based on use history on a field-by-field basis.

Fig. 7b shows the daily estimate of water use over different fields in the irrigation district obtained using Landsat 8 data acquired on 6 July 2013. Even on a daily basis, there is high variability in the rate of evapotranspiration occurring over alfalfa fields. An individual farmer could use water use information for his/her field to understand the relationship between water application and yield for improved management of the land. The daily ET image helps explain part of the spatial variability of the annual ET. For example, one can see that only half or a quarter of the center-pivot is actively irrigated on some of the fields in the July 6 image, which would lead to an overall reduction in the annual ET for that part of the field (Fig. 7).

To understand further how irrigated croplands (center-pivots) are captured by the Landsat thermal data and corresponding ET estimates, we analyzed two sample center-pivot fields. Even within the field, variation in surface temperature and ET can be captured by the SSEBop model (Fig. 8). This figure shows the spatial variation in Ts and ETa captured by Landsat 8 and Landsat 7 acquired just 8 days apart on 24 September 2013 and 2 October 2013, respectively. First, difference in the spatial resolution of the thermal band in Landsat 8 (100 m spatial resolution) compared to Landsat 7 (60 m spatial resolution) is visually apparent in Fig. 8 as there is not much sub-field variability in Ts from Landsat 8. Second, though there was little difference between Ts on these two dates, there was a relatively large difference in ETa, due to the higher reference ET on 24 September (≈ 5 mm) as compared to reference ET on 2 October (≈ 4 mm).

4.4.1. Analysis of ET by irrigation district

One of the main goals of this study was to use Landsat data to quantify water use estimates for cropland areas, especially irrigated fields. The resolution of Landsat data enables us to identify and distinguish individual irrigated fields. In this study, we analyzed annual water use estimates for five irrigation districts in the Lower CRB. The results of mean annual evapotranspiration estimates for the irrigation districts are presented in Table 4. The locations of the five irrigation districts are shown in Fig. 1. The area of each irrigation district ranges from 8273 ha (San Simon) to nearly 60,000 ha (Eloy). The mean crop ET for these districts



**Fig. 4.** Comparison of the SSEBop modeled Landsat 8 evapotranspiration estimates and measured data from two flux tower sites (Kendall grassland and Santa Rita mesquite) (a) daily (dates of Landsat overpasses) and (b) monthly.

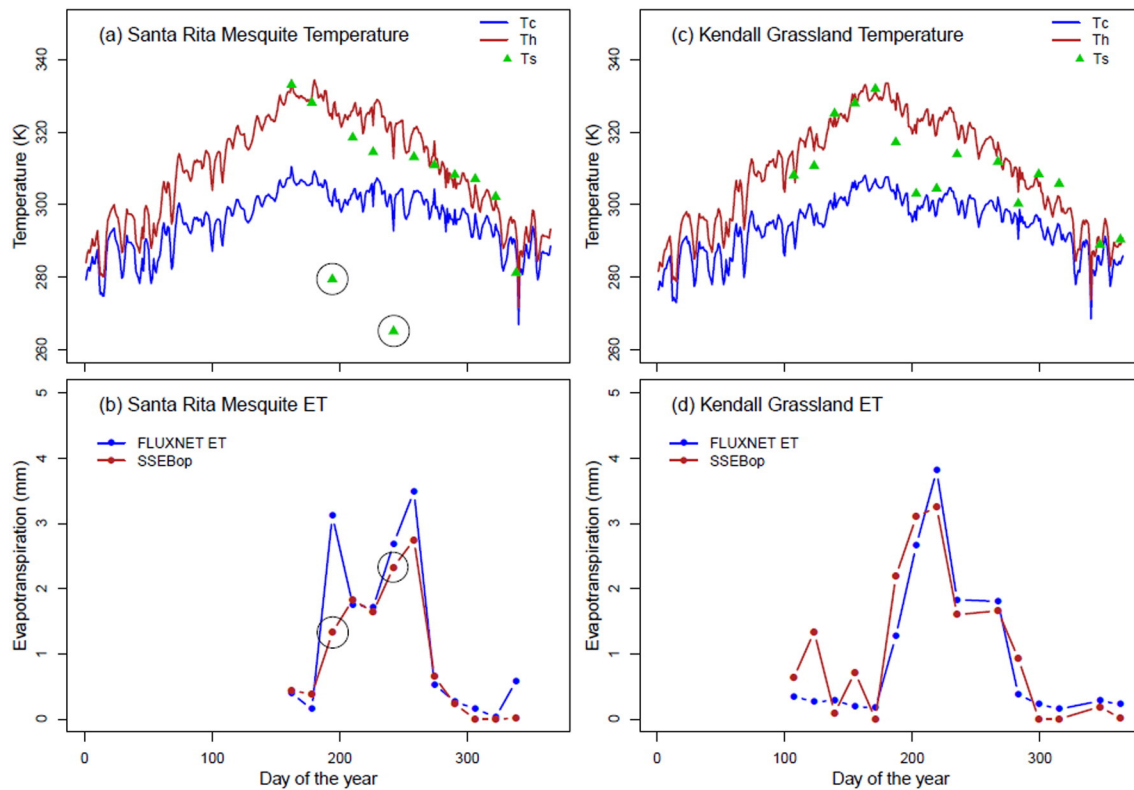


**Fig. 5.** Temporal variation of cold/wet temperature ( $T_c$ ), hot/dry temperature ( $T_h$ ), land surface temperature ( $T_s$ ) (upper panels), and measured and estimated evapotranspiration (lower panels) at two sites, the Kendall grassland and Santa Rita mesquite sites. Also shown are two cloudy dates (day of year: 194 and 242) at the Santa Rita mesquite site with circled  $T_s$  points (a) and interpolated  $ET_a$  values (b).

is comparable, ranging from 681 mm/year (San Simon) to 772 mm/year (Gila River Indian Reservation). In order to understand the amount of ET contributed by rainfall and the amount of ET actually coming from other sources such as irrigation, we summarized mean annual precipitation and the difference between evapotranspiration and precipitation ( $ET - P$ ) for each irrigation district. These irrigation districts are located in the semiarid to arid regions of the CRB where precipitation is low (<250 mm/year). Thus, considering other variables such as  $Q$  and  $\Delta S$  as negligible, we assumed that  $ET - P$  would be equal to the amount of water used for irrigation. This is particularly reasonable for the Lower CRB region as most of the precipitation is lost to evaporation, leaving negligible amounts for runoff. For example, USGS streamflow summarized for the Maricopa Stanfield irrigation district is about 0.1% of the annual

rainfall. The results indicated that  $ET - P$  for different irrigation districts ranges from 63 to 74% of the total ET (Table 4).

4.4.2. Summary of annual water use estimates for irrigated croplands

To understand the dynamics of annual water use from irrigation, we analyzed annual actual ET estimates from the irrigated fields within the Maricopa-Stanfield irrigation district. The spatial distribution of annual ET and annual  $ET - P$  over the irrigation district is presented in Fig. 9. The summary of annual ET, precipitation and  $ET - P$  for 10 major crops (by area) within the district is presented in Table 5. Mean annual ET does not just represent the ET from the crop (May–September), but also ET from other months. In 2013, alfalfa was the major crop by area covering about 36% of the irrigation district. The mean ET from the alfalfa fields (990 mm) was found to be higher than

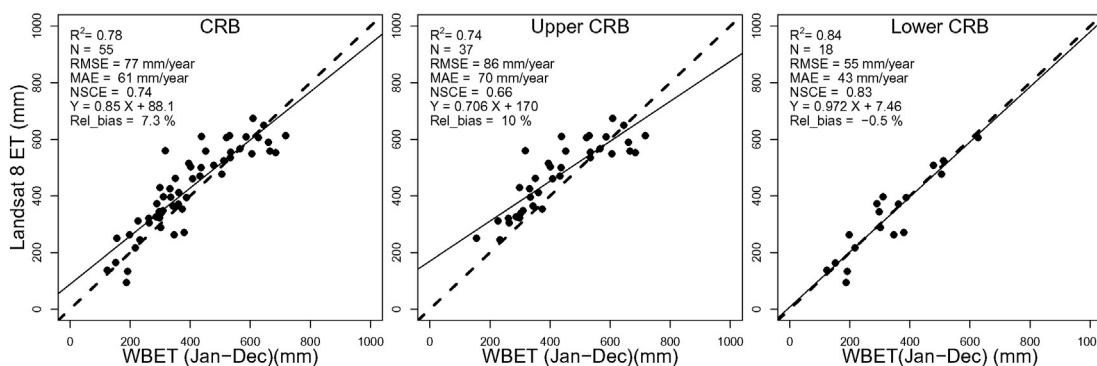


**Fig. 6.** Comparison of the annual SSEBop modeled evapotranspiration with the annual evapotranspiration based on water balance (precipitation–runoff) for the selected sub-basins within the Upper and Lower Colorado River Basins.

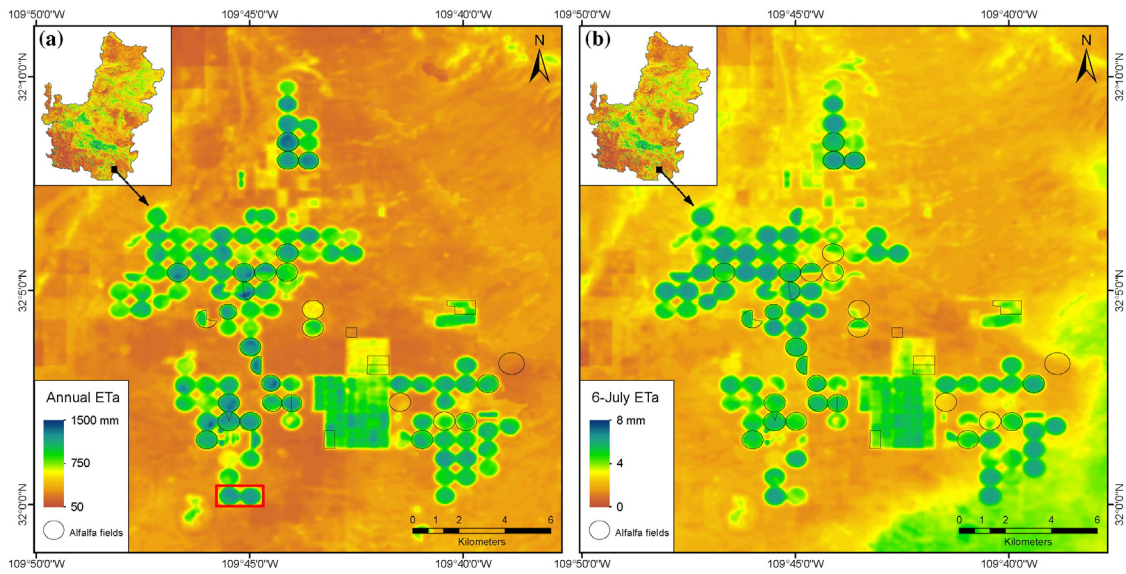


**Fig. 7.** Zoomed-in view of the spatial distribution of (a) annual evapotranspiration (mm/year) and (b) evapotranspiration (mm/day) on the day of satellite overpass (6 July 2013) within a selected part of the Southern Willcox irrigation district. Alfalfa field boundaries area overlaid to compare inter and intra-field variability in ET. A zoomed-in view of the area in the red box is presented in Fig. 8. (For interpretation of the reference to color in this figure, the reader is referred to the web version of this article.)

other crops. Other irrigated fields such as corn, double crop (barley/sorghum), and cotton fields also showed high annual ET. Precipitation over the irrigation district is about 200 mm/year and only supports about 20% of the annual ET. The indication of consumptive water use from irrigation ( $ET - P$ ) varies at about 70–80% for major irrigated crop fields as indicated in Table 5.

**4.5. Opportunities and challenges of using Landsat images for consumptive water use estimation**

A clear advantage of Landsat-based ET mapping is the capability to quantify water use at a field scale where ET maps can be used for water management purposes. However, the high spatial resolution of

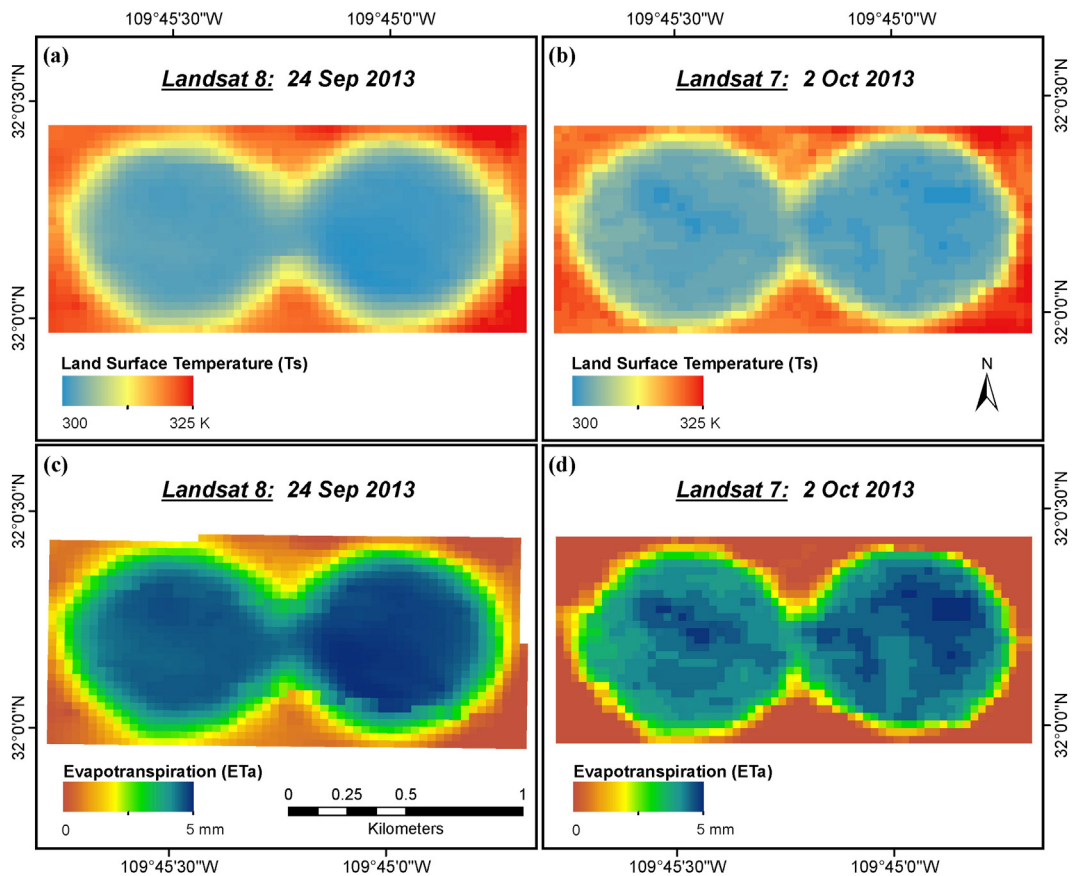


**Fig. 8.** Zoomed-in view of the land surface temperature and evapotranspiration estimated over two selected center pivot irrigation systems (red box in Fig. 7a) for 24 September 2013 and 2 October 2013, acquired using Landsat 8 (100 m spatial resolution) and Landsat 7 (60 m spatial resolution), respectively.

**Table 4**

Summary of 2013 total evapotranspiration, precipitation, and irrigation based ET over five irrigation districts in the Colorado River Basin.

S. No	Irrigation district	Area (ha)	Crop ET		Precipitation		Irrigation based ET ( $ET - P$ )		
			Mean	Total	Mean	Total	Mean	Total	%ET
			mm/year	ha-m	mm/year	ha-m	mm/year	ha-m	
1	Willcox	25,344	765	19,396	251	6365	514	13,031	67
2	San Simon	8273	681	5636	250	2071	431	35,64	63
3	Maricopa Stanfield	33,062	768	25,376	196	6481	571	18,895	74
4	Gila River Indian Reservation	14,474	772	11,170	213	3078	559	8093	72
5	Eloy	59,580	744	44,346	228	13,566	517	30,780	69

Landsat comes at the cost of a reduced temporal frequency and limited swath width. Because of cloud cover, particularly during the growing season, the 16-day Landsat 8 repeat cycle could easily extend to 32 days or more, requiring interpolation between image dates that would likely increase uncertainty. For example, Fig. 5 shows that only one (DOY 242) of the two cloudy days (DOY: 194 & 242) at the Santa Rita mesquite flux site has been interpolated reasonably. Although the Fmask algorithm has enabled the detection and masking of most clouds, the range of top of atmosphere (TOA) reflectance values from two-way water vapor path lengths in the cirrus band remains challenging for cloud detection of high altitude clouds over bright surfaces in dry environments. In order to reduce commission errors and misidentification as clouds, a relatively large threshold of the cirrus band is required in the algorithm, but this will also exclude some of the thin cirrus clouds (Zhu, Wang, & Woodcock, 2015). Noise from haze-like semi-transparent cirrus clouds is evident in Fig. 7b where the southeastern portion of the image on 6 July 2013 appears as modeled ET relating to cool land surface temperature not captured by the TOA reflectance threshold. A separate examination of the  $T_s$  image (not shown) clearly indicates a shadowy hazy pattern in the Landsat image acquired on 6 July 2013. Yu et al. (2015) also reported that human interpretation is more accurate than an automated algorithm (Fmask) to identify clouds and cloud shadows.

A related challenge with clouds and infrequent coverage with Landsat is the unequal number of images used to create seasonal/annual ET. For example, (Singh, Senay, Velpuri, Bohms, Scott, et al., 2014) used 328 images (an average of 7.6 images per path/row) using <10% cloud threshold to create an annual total for the Colorado River Basin, and in this study we used 528 images (an average of 12.3 images per path/row, <60% cloud threshold) with a desire to include as many good

(non-cloud) pixels in an image. Partly attributable to these differences, the seasonal ET from the two years could not be compared directly in absolute terms. However, an opportunity exists in merging Landsat with MODIS to improve cloud-filling (Singh, Senay, Velpuri, Bohms & Verdin, 2014). To reduce the impact of interpolation errors between cloudy scenes, future work could include merging Landsat and MODIS to create 8-day ET at the Landsat scale.

Furthermore, the relatively smaller swath width of Landsat (185 km) compared to other coarse images such as MODIS (2330 km) necessitates a large number of images to be processed and merged to create a seamless product. Creating a seamless annual/seasonal product by combining different processed images is challenging particularly for the overlapped areas between two paths/rows as different paths/rows may be based on different numbers of Landsat images. In the pioneering work of Bastiaanssen et al. (1998), and later adopted by Allen et al. (2007) and Senay et al. (2007), each image requires its own hot and cold reference values to estimate ET using a surface energy balance approach in SEBAL/METRIC and a simplified version in SSEB. The challenge with the image-specific hot and cold pixel approach is that each set of hot and cold pixels is only valid for a uniform hydro-climatic landscape comparable to the reference pixels and not for the entire image, requiring more conditioning of the  $T_s$ , for example, to account for elevation differences.

To create a seamless ET across varied hydro-climatic regions and Landsat scenes, the SSEBop model in Senay et al. (2013) introduced an empirical approach to estimate the crucial parameter of differential temperature between the hot and cold pixels ( $dT$ ) using a daily average clear-sky net radiation. In SSEBop formulation, hot and cold limits are defined on the same pixel; therefore,  $dT$  actually represents the vertical temperature difference between the surface temperature of a

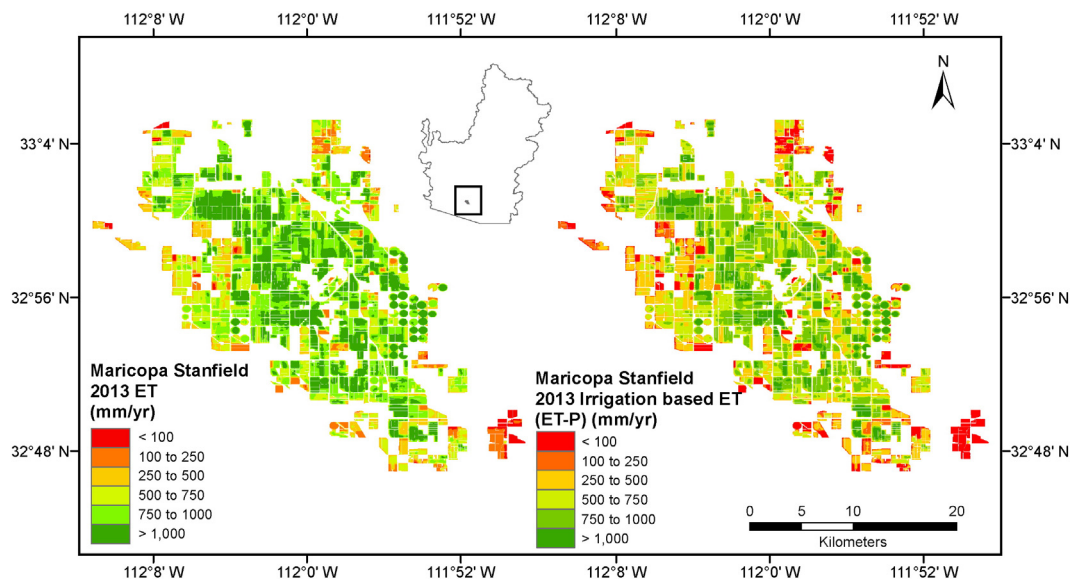


**Fig. 9.** Illustration of annual evapotranspiration (mm/year) using Landsat 8 images based on the SSEBop model (left) and irrigation-based evapotranspiration ( $ET - Precipitation$ ) (right) over the Maricopa Stanfield irrigation district.

**Table 5**  
Summary of actual evapotranspiration of selected croplands within the Maricopa Stanfield irrigation district for 2013.

S.No	Land cover	Area (%)	Mean annual ET (mm)	Mean annual Precip (mm)	(ET – P) annual (mm)	(ET – P) annual (%)
1	Alfalfa	36.34	990	198	792	80
2	Corn	16.64	966	196	770	80
3	Cotton	13.32	765	192	573	75
4	Barley	10.20	661	199	462	70
5	Fallow/idle cropland	8.39	275	197	77	28
6	Cantaloupes	4.52	560	189	372	66
7	Sorghum	2.19	744	203	541	73
8	D1 crop barley/sorghum	2.03	963	192	771	80
9	Durum wheat	1.25	384	200	184	48
10	Other hay/non-alfalfa	1.02	833	197	635	76

theoretical bare/dry condition of a given pixel and the air temperature at the canopy level of the same pixel. The linear relationship between daily average net radiation and  $dT$  is shown in Fig. 10 for the Kendall grassland site. Although the temperature difference shown in Fig. 10 is between soil temperature ( $T_{\text{soil}}$ ) at the 5-cm depth underlying a grass vegetation and air temperature, compared to the desired bare-ground surface temperature in the SSEBop formulation, a reasonable linear relationship ( $R^2 = 0.73$ ) supports the validity of using a daily average net-radiation to estimate the hot and cold pixel difference at the time of satellite overpass. To simulate the bare and dry ground surface conditions, only days with an average latent heat-flux of less than 20% of the net-radiation were used. The 20% threshold is used to include as many days in the relationship while avoiding days with substantial rainfall and soil moisture that will reduce surface temperature. Despite the expected confounding factors from the observed latent heat-flux and soil temperature (5 cm below the surface) measurements, 73% of the daily variation in “ $dTs$ ” was explained by the daily-average net radiation in 2013. This finding strengthens the assumption of the SSEBop approach where each pixel is treated individually with its own theoretical  $dT$ , allowing the approach to create seamless ET over large regions. The temporal evolution of the  $dT$  ( $T_h - T_c$ ) and its relationship with  $T_s$  for the Kendall grassland eddy covariance tower site is intuitive (Fig. 5). The simplicity of plotting and interpreting  $T_s$  between  $T_h$  and  $T_c$  is obvious for operational implementation.

Furthermore, this study also highlights the importance of combining overpass date ET estimation along with seasonal ET estimation in order

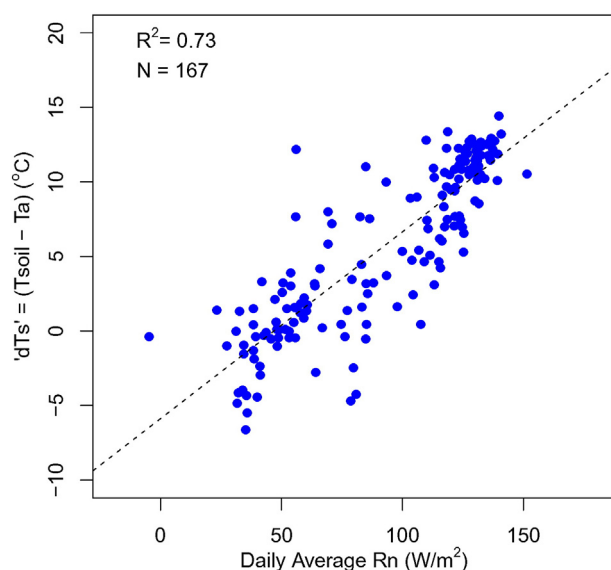


**Fig. 10.** Scatterplot showing the empirical relationship between daily averaged net radiation and difference of maximum daily soil temperature (5 cm below surface) and maximum daily air temperature at the Kendall grassland flux site for 2013.  $N$  = days when daily latent heat flux is  $<20\%$  of daily net radiation.

to understand the sources of spatial variation in ET. As shown in Fig. 7, the same land cover tends to have high spatial variability among irrigated fields, yet the main cause for this appears to be related to variability in land and water management practices during the cropping season.

Thus, despite the challenges of clouds and multi-scene processing, new tools in cloud computing platforms such as Google Earth Engine for merging Landsat with MODIS and innovative modeling approaches have a great potential not only for estimating crop water use routinely but also for understanding the impact of management on the seasonal crop water use. A follow-up study is planned and recommended to conduct a multi-year modeling using uniform methodology and criteria so that historical and current images from Landsat 5, 7 and 8 will be used to produce seamless and temporally consistent seasonal water use maps.

## 5. Conclusions

Information on water use and water availability at the field and basin scale is important in water resource assessment, development, and management. Such information is needed, particularly in dry areas such as the Southwest United States. We carried out a water use assessment of the Colorado River Basin in the Southwest United States for 2013 using 528 images from the Landsat 8 satellite. The Operational Simplified Surface Energy Balance (SSEBop) model was used for computing evapotranspiration using Landsat 8 and other ancillary data. The validation of results using eddy covariance data from the Kendall grassland and Santa Rita mesquite sites showed good agreement at both sites for the days of satellite overpasses ( $R^2 = 0.82$ ) as well as for monthly ET ( $R^2 = 0.85$  to  $0.91$ ). A comparison between the SSEBop-modeled ET and the water balance-based ET for selected sub-basins (hydrologic unit code 8) showed encouraging results both in the Upper and Lower Colorado River Basins. Water use distribution among various land use/land cover showed that cropland has consumed, a spatially averaged depth of  $726 \text{ mm year}^{-1}$  with a standard deviation of  $372 \text{ mm}$ , second only to open water bodies ( $1223 \pm 495 \text{ mm/year}$ ). Because of their large area coverage, shrublands consumed the largest amount of volumetric water at  $146 \text{ km}^3$  followed by evergreen forest ( $78 \text{ km}^3$ ) and grasslands ( $16 \text{ km}^3$ ) which are by far the largest users of water in comparison to croplands at  $4 \text{ km}^3$ . However, croplands are the largest consumer of blue water while shrublands consumed the most green water in CRB.

Furthermore, the contribution of rainfall appears to fall in the range of 26–43% of the total crop consumptive use in the five irrigation districts in the Lower Colorado River Basin. A relatively large variation in the contribution of rainfall highlights the importance of identifying and quantifying ET sources as rainfall versus irrigation for improved management in irrigation system design and water allocation.

The spatial distribution and accuracy of the SSEBop evapotranspiration estimates across the Colorado River Basin illustrate the usefulness and tremendous potential of Landsat 8 for water management purposes. With this study, we were able to successfully leverage the capacity of such satellite information in a way that can provide both

integrative and quantitative visual and analytical components for the study of water use and availability. An understanding and advancement of modeling capabilities associated with these directives help promote the value of remote sensing technologies for next generation ET modeling initiatives, and the powerful information resulting from that. More than 40 years of Landsat legacy can be instrumental in identifying and recording water footprints of different fields. Furthermore, our approach can be used in estimating historical water use at the field level and in quantifying the impact of climate change and land use conversion on water use. Future research will continue to focus on efforts to processing all historical and current Landsat images with consistent methodology and criteria in support of the USGS National Water Census research program.

## Acknowledgments

This work was performed under the United States Geological Survey (USGS) contracts G13PC00028 and G10PC00044 in support of the WaterSMART program. We gratefully acknowledge the use of flux data supplied by Dr. Russell Scott, Agricultural Research Service, U.S. Department of Agriculture for our model validation. We also thank Saeid Tadayon and Amy Read from the USGS Arizona Water Science Center for sharing geospatial data of five irrigation districts. We thank and express our sincere appreciation to the three anonymous reviewers for their constructive comments and suggestions to improve the manuscript. Any use of trade, firm, or product names is for descriptive purposes only and does not imply endorsement by the U.S. Government.

## References

- Allen, R. G., Pereira, L. S., Howell, T. A., & Jensen, M. E. (2011). Evapotranspiration information reporting: I. Factors governing measurement accuracy. *Agricultural Water Management*, 98, 899–920.
- Allen, R. G., Pereira, L. S., Raes, D., & Smith, M. (1998). *Crop evapotranspiration—Guidelines for computing crop water requirements—FAO irrigation and drainage paper 56*. 300, Rome: FAO.
- Allen, R. G., Tasumi, M., & Trezza, R. (2007). Satellite-based energy balance for mapping evapotranspiration with internalized calibration (METRIC)—Model. *Journal of Irrigation and Drainage Engineering*, 133, 380–394.
- Anderson, M. C., Norman, J. M., Mecikalski, J. R., Otkin, J. A., & Kustas, W. P. (2007). A climatological study of evapotranspiration and moisture stress across the continental United States based on thermal remote sensing: 1. Model formulation. *Journal of Geophysical Research—Atmospheres*, 1984–2012, 112.
- Baldocchi, D., Falge, E., Gu, L., Olson, R., Hollinger, D., Running, S., ... Evans, R. (2001). FLUXNET: A new tool to study the temporal and spatial variability of ecosystem-scale carbon dioxide, water vapor, and energy flux densities. *Bulletin of the American Meteorological Society*, 82, 2415–2434.
- Bastiaanssen, W., Menenti, M., Feddes, R., & Holtslag, A. (1998). A remote sensing surface energy balance algorithm for land (SEBAL). 1. Formulation. *Journal of Hydrology*, 212, 198–212.
- Boryan, C., Yang, Z., Mueller, R., & Craig, M. (2011). Monitoring US agriculture: The US Department of Agriculture, National Agricultural Statistics Service, Cropland Data Layer program. *Geocarto International*, 26, 341–358.
- Daly, C., Smith, J. W., Smith, J. L., & McKane, R. B. (2007). High-resolution spatial modeling of daily weather elements for a catchment in the Oregon Cascade Mountains, United States. *Journal of Applied Meteorology and Climatology*, 46, 1565–1586.
- Daly, C., Taylor, G., Gibson, W., Parzybok, T., Johnson, G., & Pasteris, P. (2000). High-quality spatial climate data sets for the United States and beyond. *Transactions of the ASAE—American Society of Agricultural Engineers*, 43, 1957–1962.
- Di Luzio, M., Johnson, G., Daly, C., Eischeid, J., & Arnold, J. (2008). Constructing retrospective gridded daily precipitation and temperature datasets for the conterminous United States. *Journal of Applied Meteorology and Climatology*, 47, 475–497.
- DOI, United States Department of Interior (2011). Fiscal Year 2011 The Interior Budget in Brief. *WaterSMART: Departmental highlights* (pp. 19–25).
- Farr, T. G., & Kobrick, M. (2000). Shuttle Radar Topography Mission produces a wealth of data. *Eos, Transactions American Geophysical Union*, 81, 583–585.
- Fisher, J. B., Whittaker, R. J., & Malhi, Y. (2011). ET come home: Potential evapotranspiration in geographical ecology. *Global Ecology and Biogeography*, 20, 1–18.
- Glenn, E. P., Neale, C. M., Hunsaker, D. J., & Nagler, P. L. (2011). Vegetation index-based crop coefficients to estimate evapotranspiration by remote sensing in agricultural and natural ecosystems. *Hydrological Processes*, 25, 4050–4062.
- Gowda, P., Chavez, J., Colaizzi, P., Evett, S., Howell, T., & Tolk, J. (2007). Remote sensing based energy balance algorithms for mapping ET: Current status and future challenges. *Transactions of the ASABE*, 50, 1639–1644.
- Holland, T. (1992). Water-use data collection techniques in the southeastern United States, Puerto Rico, and the US Virgin Islands: Little Rock, Ark. *US Geological Survey Water-Resources Investigations Report 92–4028* (195 pages).
- Huang, C., Thomas, N., Goward, S. N., Masek, J. G., Zhu, Z., Townshend, J. R., & Vogelmann, J. E. (2010). Automated masking of cloud and cloud shadow for forest change analysis using Landsat images. *International Journal of Remote Sensing*, 31, 5449–5464.
- Irish, R. R., Barker, J. L., Goward, S. N., & Arvidson, T. (2006). Characterization of the Landsat-7 ETM+ automated cloud-cover assessment (ACCA) algorithm. *Photogrammetric Engineering & Remote Sensing*, 72, 1179–1188.
- Irons, J. R., Dwyer, J. L., & Barsi, J. A. (2012). The next Landsat satellite: The Landsat data continuity mission. *Remote Sensing of Environment*, 122, 11–21.
- Jian, X., Wolock, D., & Lins, H. (2008). *WaterWatch—Maps, graphs, and tables of current, recent, and past streamflow conditions, United States Geological Survey, electronic resource*. (accessed April 21, 2015 at) <http://pubs.usgs.gov/fs/2008/3031/WaterWatch2008v3.pdf>
- Jin, S., Yang, L., Danielson, P., Homer, C., Fry, J., & Xian, G. (2013). A comprehensive change detection method for updating the National Land Cover Database to circa 2011. *Remote Sensing of Environment*, 132, 159–175.
- Kalma, J. D., McVicar, T. R., & McCabe, M. F. (2008). Estimating land surface evaporation: A review of methods using remotely sensed surface temperature data. *Surveys in Geophysics*, 29, 421–469.
- Landerer, F., & Swenson, S. (2012). Accuracy of scaled GRACE terrestrial water storage estimates. *Water Resources Research*, 48.
- Loheide, S. P., & Gorelick, S. M. (2005). A local-scale, high-resolution evapotranspiration mapping algorithm (ETMA) with hydroecological applications at riparian meadow restoration sites. *Remote Sensing of Environment*, 98, 182–200.
- Maiersperger, T., Scaramuzza, P., Leigh, L., Shrestha, S., Gallo, K., Jenkerson, C., & Dwyer, J. (2013). Characterizing LEDAPS surface reflectance products by comparisons with AERONET, field spectrometer, and MODIS data. *Remote Sensing of Environment*, 136, 1–13.
- Mann, W., Moore, J., & Chase, E. (1982). A national water-use information program. *U.S. Geological Survey Open-File Report 82–862* (pp. 18).
- Masek, J. G., Vermote, E. F., Saleous, N. E., Wolfe, R., Hall, F. G., Huemmrich, K. F., ... Lim, T. -K. (2006). A Landsat surface reflectance dataset for North America, 1990–2000. *Geoscience and Remote Sensing Letters, IEEE*, 3, 68–72.
- Maupin, M. A., Kenny, J. F., Hutson, S. S., Lovelace, J. K., Barber, N. L., & Linsey, K. S. (2014). Estimated use of water in the United States in 2010. *U.S. Geological Survey Circular*. 1405. (pp. 56). <http://dx.doi.org/10.3133/cir1405>.
- Menenti, M., & Choudhury, B. J. (1993). Parameterization of land surface evaporation by means of location dependent potential evaporation and surface temperature range. In H. J. Bolle, R. A. Feddes, & J. D. Kalma (Eds.), *Exchange process at the land surface for a range of space and time scales, publication no. 212* (pp. 561–568). UK: International Association of Hydrological Sciences.
- Norman, J. M., Kustas, W. P., & Humes, K. S. (1995). Source approach for estimating soil and vegetation energy fluxes in observations of directional radiometric surface temperature. *Agricultural and Forest Meteorology*, 77, 263–293. [http://dx.doi.org/10.1016/0168-1923\(95\)02265-Y](http://dx.doi.org/10.1016/0168-1923(95)02265-Y).
- Roerink, G., Su, Z., & Menenti, M. (2000). S-SEBI: A simple remote sensing algorithm to estimate the surface energy balance. *Physics and Chemistry of the Earth, Part B: Hydrology, Oceans and Atmosphere*, 25, 147–157.
- Roy, D. P., Ju, J., Kline, K., Scaramuzza, P. L., Kovalskyy, V., Hansen, M., ... Zhang, C. (2010). Web-enabled Landsat Data (WELD): Landsat ETM+ composited mosaics of the conterminous United States. *Remote Sensing of Environment*, 114, 35–49.
- Schaaf, C. B., Gao, F., Strahler, A. H., Lucht, W., Li, X., Tsang, T., ... Muller, J. -P. (2002). First operational BRDF, albedo nadir reflectance products from MODIS. *Remote Sensing of Environment*, 83, 135–148.
- Scott, R. L. (2010). Using watershed water balance to evaluate the accuracy of eddy covariance evaporation measurements for three semiarid ecosystems. *Agricultural and Forest Meteorology*, 150, 219–225.
- Scott, R. L., Hamerlynck, E. P., Jenerette, G. D., Moran, M. S., & Barron-Gafford, G. A. (2010). Carbon dioxide exchange in a semidesert grassland through drought-induced vegetation change. *Journal of Geophysical Research: Biogeosciences (2005–2012)*, 115.
- Scott, R. L., Jenerette, G. D., Potts, D. L., & Huxman, T. E. (2009). Effects of seasonal drought on net carbon dioxide exchange from a woody-plant-encroached semiarid grassland. *Journal of Geophysical Research: Biogeosciences (2005–2012)*, 114.
- Seaber, P. R., Kapinos, F. P., & Knapp, G. L. (1987). *Hydrologic unit maps*. accessed Apr 21, 2015 at <http://pubs.usgs.gov/wsp/wsp2294/index.html>
- Senay, G., Leake, S., Nagler, P., Artan, G., Dickinson, J., Cordova, J., & Glenn, E. (2011). Estimating basin scale evapotranspiration (ET) by water balance and remote sensing methods. *Hydrological Processes*, 25, 4037–4049.
- Senay, G., Velpuri, N., Bohms, S., Demissie, Y., & Gebremichael, M. (2014). Understanding the hydrologic sources and sinks in the Nile Basin using multisource climate and remote sensing data sets. *Water Resources Research*, 50, 8625–8650.
- Senay, G., Verdin, J., Lietzow, R., & Melesse, A. (2008). *Global daily reference evapotranspiration modeling and evaluation 1*. Wiley Online Library.
- Senay, G. B., Bohms, S., Singh, R. K., Gowda, P. H., Velpuri, N. M., Alemu, H., & Verdin, J. P. (2013). Operational evapotranspiration mapping using remote sensing and weather datasets: A new parameterization for the SSEB approach. *JAWRA Journal of the American Water Resources Association*, 49, 577–591.
- Senay, G. B., Budde, M., Verdin, J. P., & Melesse, A. M. (2007). A coupled remote sensing and simplified surface energy balance approach to estimate actual evapotranspiration from irrigated fields. *Sensors*, 7, 979–1000.
- Serbina, L. O., & Miller, H. M. (2014). Landsat and water: Case studies of the uses and benefits of Landsat imagery in water resources. *U.S. Geological Survey Open-File Report 2014–1108* (pp. 61).
- Singh, R. K., & Irmak, A. (2011). Treatment of anchor pixels in the METRIC model for improved estimation of sensible and latent heat fluxes. *Hydrological Sciences Journal*, 56, 895–906.

- Singh, R. K., Senay, G. B., Velpuri, N. M., Bohms, S., & Verdin, J. P. (2014b). On the down-scaling of actual evapotranspiration maps based on combination of MODIS and Landsat-based actual evapotranspiration estimates. *Remote Sensing*, 6, 10483–10509.
- Singh, R. K., Senay, G. B., Velpuri, N. M., Bohms, S., Scott, R. L., & Verdin, J. P. (2014a). Actual evapotranspiration (water use) assessment of the Colorado River Basin at the Landsat resolution using the Operational Simplified Surface Energy Balance model. *Remote Sensing*, 6, 233–256.
- Singh, R. K., Liu, S., Tieszen, L. L., Suyker, A. E., & Verma, S. B. (2011). Estimating seasonal evapotranspiration from temporal satellite images. *Irrigation Science*, 30, 303–313. <http://dx.doi.org/10.1007/s00271-011-0287-z>.
- Sobrino, J. A., Jiménez-Muñoz, J. C., & Paolini, L. (2004). Land surface temperature retrieval from LANDSAT TM 5. *Remote Sensing of Environment*, 90, 434–440.
- Solley, W. B., Merk, C. F., & Pierce, R. R. (1988). Estimated use of water in the United States 1985. *U.S. Geological Survey Circular 1004* (pp. 82) (<http://pubs.er.usgs.gov/publication/cir1004>).
- Su, Z. (2002). The Surface Energy Balance System (SEBS) for estimation of turbulent heat fluxes. *Hydrology and Earth System Sciences Discussions*, 6, 85–100.
- Thornton, P. E., Thornton, M. M., Mayer, B. W., Wilhelmi, N., Wei, Y., Devarakonda, R., & Cook, R. B. (2014). *Daymet: Daily surface weather data on a 1-km grid for North America, Version 2. Data set*. Oak Ridge, Tennessee, USA: Oak Ridge National Laboratory Distributed Active Archive Center. <http://dx.doi.org/10.3334/ORNLDAAC/1219>.
- USBR (2015). Colorado River Basin natural flow and salt data. *Current Natural Flow and Salt Data* (accessed 04/05/2015 at <http://www.usbr.gov/lc/region/g4000/NaturalFlow/current.html>).
- Velpuri, N. M., Senay, G. B., Singh, R. K., Bohms, S., & Verdin, J. P. (2013). A comprehensive evaluation of two MODIS evapotranspiration products over the conterminous United States: Using point and gridded FLUXNET and water balance ET. *Remote Sensing of Environment*, 139, 35–49.
- Wilson, K., Goldstein, A., Falge, E., Aubinet, M., Baldocchi, D., Berbigier, P., ... Field, C. (2002). Energy balance closure at FLUXNET sites. *Agricultural and Forest Meteorology*, 113, 223–243.
- Wukelic, G., Gibbons, D., Martucci, L., & Foote, H. (1989). Radiometric calibration of Landsat Thematic Mapper thermal band. *Remote Sensing of Environment*, 28, 339–347.
- Yu, L., Ball, S. B., Blinn, C. E., Moeltner, K., Peery, S., Thomas, V. A., & Wynne, R. H. (2015). Cloud-Sourcing: Using an online labor force to detect clouds and cloud shadows in Landsat images. *Remote Sensing*, 7, 2334–2351.
- Zhang, K., Kimball, J. S., Nemani, R. R., & Running, S. W. (2010). A continuous satellite-derived global record of land surface evapotranspiration from 1983 to 2006. *Water Resources Research*, 46, W09522. <http://dx.doi.org/10.1029/2009WR008800>.
- Zhu, Z., & Woodcock, C. E. (2012). Object-based cloud and cloud shadow detection in Landsat imagery. *Remote Sensing of Environment*, 118, 83–94.
- Zhu, Z., Wang, S., & Woodcock, C. E. (2015). Improvement and expansion of the Fmask algorithm: Cloud, cloud shadow, and snow detection for Landsats 4–7, 8, and Sentinel 2 images. *Remote Sensing of Environment*, 156, 269–277.